Influence of Inner Surface Roughness on the Spectral Induced Polarization Response—A Numerical Study

E. Zibulski[1] and **N. Klitzsch[1]**

[1]Computational Geoscience, Geothermics and Reservoir Geophysics, RWTH Aachen, Aachen, Germany

Abstract Spectral induced polarization (SIP) laboratory measurements on water-saturated rocks show a strong correlation between the electrical polarization strength and the inner surface area of rocks. We investigate the influence of inner surface roughness on the SIP response by simulating the frequency-dependent complex conductivity of micro-scale rock models. Starting with smooth grain models, we introduce surface roughness using two different approaches: increasing the surface roughness in a fractal-like manner, and creating random surface structures, resulting in more natural-looking surfaces. We find that surface roughness has two distinct effects on the SIP response: (a) a shift in the position and magnitude of the primary relaxation frequency to lower frequencies and lower magnitudes, respectively, and (b) the formation of secondary polarizations above the polarization frequency of the primary polarization. We also compare the relaxation time and normalized chargeability obtained by Debye decomposition and the imaginary conductivity at 1 Hz of our models with mechanistic models and empirical relations. We point out the congruences and offer explanations for the discrepancies between our models and the empirical observations. We conclude that the results of our study are applicable to real rocks and that the SIP method has the potential to detect inner surface roughness. However, the SIP method it not able to discriminate between signals from rough particles and a distribution of smooth particles.

Plain Language Summary The spectral induced polarization method measures the electrical conductivity of the subsurface at depths of investigation ranging from a few dm to several 100 m. The potential of the method to detect mineral resources, contamination, microbial activity, etc. makes it a promising tool for today's environmental challenges. However, due to the complexity of the underlying physical and chemical processes the interpretation of SIP measurements often remains qualitative. Mathematical and mechanistic models used to describe the processes are usually simplified with respect to geometry, chemistry, and physical properties. In this study, we use computer simulations to investigate the surfaces of spherical particles (grains). After simulating the SIP response of models with smooth and rough surfaces, we analyze the influence of surface roughness on the SIP response. We find that surface roughness causes distinct changes in the SIP response compared to the smooth grain. However, we also find that this introduces an ambiguity in the interpretation of SIP data.

1. Introduction

Geoelectrical methods, such as electrical resistivity tomography (ERT) and electromagnetic methods, measure the electrical conductivity of the subsurface at depths of investigation ranging from a few dm to several 100 m. The spectral induced polarization (SIP) method measures the frequency-dependent complex electrical conductivity σ^* of rocks as a function of frequency, typically in the mHz to kHz range. Schlumberger (1920) discovered an induced polarization (IP) effect during the time domain geoelectrical field experiments, giving the method its name. This method makes use of a capacitive effect, indicated by a slow voltage decay after the current is turned off. The voltage decay measured in the time domain corresponds to a phase shift between current and potential in the frequency domain.

As in conventional resistivity measurements, a typical configuration for measuring the complex electrical conductivity involves four electrodes. Two electrodes inject an AC current into the ground and the electrical potential is measured between the two other electrodes (Figure 1). The current electrodes inject an AC current $I^* = |I|exp(j(\omega t + \phi_I))$ with an angular frequency $\omega = 2\pi f$, where $j = \sqrt{-1}$, t is time, and ϕ_I is the current phase.
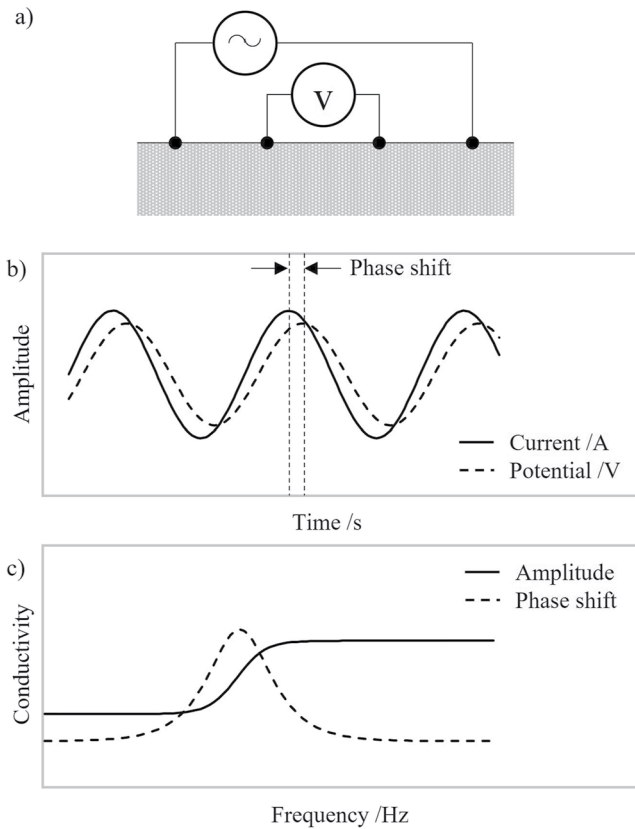
a)

b)

c)

Figure 1. (a) Schematic of the field measurement and (b) the readouts of the injected AC current and measured electric potential in the time domain. Repeating this measurement over a range of frequencies and plotting the amplitude and phase at each frequency gives (c) the frequency-dependent response.

Simultaneously, we measure the amplitude $|U|$ and the phase ϕ_U of the electric potential between the two other electrodes:

$$U^* = |U|\exp(j(\omega t + \phi_U)) \tag{1}$$

In SIP we repeat this measurement over a range of frequencies, usually between 10^{-3}–10^5 Hz in the laboratory and 10^{-2}–10^2 Hz in the field. We can then calculate the frequency-dependent electrical impedance of the sample at each sampled frequency with

$$Z^*(\omega) = \frac{|U|}{|I|}\exp(j(\phi_U - \phi_I)) \tag{2}$$

From the complex electrical impedance, we can calculate the complex electrical resistivity using the geometric factor K as for DC measurements:

$$\rho^*(\omega) = Z^*(\omega) \cdot K \tag{3}$$

Electrical resistivity ρ and electrical conductivity σ are related by $\rho = 1/\sigma$. Typically, instead of working with the amplitude and phase of the complex conductivity we would use the real conductivity σ' and the imaginary conductivity σ'' of the complex valued electrical conductivity $\sigma^*(\omega) = \sigma'(\omega) + j\sigma''(\omega)$. More information about IP measurements in time and frequency domain can be found, for example, in Telford et al. (1990).

Since the electrical conductivity of porous rocks (without conductive constituents) depends on many parameters (Archie, 1942), the interpretation of the electrical conductivity mostly remains qualitative and ambiguous. The additional information obtained from complex conductivity measurements make the SIP method promising for reducing the ambiguity of the interpretation. So far, scientists and engineers have mainly exploited the sensitivity of the imaginary part of the conductivity to the properties of the inner surface, the interface between the solid rock matrix and the pore filling fluid. For example, the SIP method was applied for hydrogeophysical (e.g., Hördt et al., 2009; Weller & Börner, 1996) and biogeophysical problems (e.g., Atekwana & Slater, 2009; Flores Orozco et al., 2011; Mellage et al., 2018). For the hydrogeological interpretation of SIP measurements, the hydraulic permeability is estimated using its correlation to inner surface area, which in turn depends on σ''. In biogeophysical applications, bacterial or microorganism growth happening on the inner surface has an impact on electrochemical properties and, thus, on the SIP response (Strobel et al., 2023).

The interpretation of SIP measurements often remains qualitative too, for example, because the electrochemical properties of the inner surface, usually unknown in geophysical field measurements, influence the imaginary conductivity (e.g., Revil & Skold, 2011, Weller & Breede, 2006). The quantitative interpretation of SIP measurements requires additional information that can potentially be obtained by exploiting the frequency dependence of the conductivity. However, the latter is still not fully understood and is a focus of ongoing research. Although there are mechanistic models describing the frequency dependence for several polarization mechanisms (e.g., Blaschek & Hördt, 2009; Leroy & Revil, 2009), semi-empirical relations (Cole & Cole, 1941; Pelton et al., 1978) are often used to characterize the frequency dependence.

Full exploitation of the SIP method requires universal relationships that take into account the pore space geometries and the electrochemical properties of the fluid-mineral interface. In addition, geophysicists must account for all polarization mechanisms that contribute to the frequency dependence. In total, there are five microscopic mechanisms that lead to rock polarization in the mHz to MHz frequency range.

1. electrical double layer (EDL) polarization, for example, Revil and Florsch (2010);
2. Membrane polarization, for example, Marshall and Madden (1959);
3. interfacial (Maxwell-Wagner) polarization, for example, Sen et al. (1981), Chen and Or (2006);
4. electrode polarization, only in the presence of conductive minerals, for example, Wong (1979); and

5. high-frequency polarization mechanisms such as water dipole orientation, for example, Kremer and Schönhals (2003).

In this paper, we neglect electrode polarization (4) because we only consider non-conducting minerals. Polarization mechanisms (1) and (2), both caused by the EDL, dominate in the low frequency range. For the EDL polarization (1) grain-based models have been proposed, for example, by O'Konski (1960), Schwarz (1962), and Schurr (1964). Membrane polarization (2) is a pore-based model that describes polarization as a response to charge separation in the pore space. Both approaches have been refined over the years (Bücker & Hördt, 2013a, 2013b; Titov et al., 2002). With increasing frequency, interfacial polarization (3) and high-frequency polarization mechanisms (5) become increasingly important, that is, the four polarization mechanisms operate in overlapping frequency ranges (Revil, 2013).

In this study we focus on the polarization mechanism (1). The corresponding models provide information on chargeability m, the normalized difference between high- and low-frequency conductivities, and a distribution of relaxation times for the potential decay, which is associated with a distribution of polarization length scales. These length scales are related to the grain size or characteristic pore size (Revil et al., 2012). However, these relationships are based on simplified assumptions about the microstructure and processes at the solid-water interface. Typically, we consider ideal geometric shapes (e.g., spheres, cylinders) with smooth surfaces. Expectedly, such simplified models have their shortcomings for the analysis of SIP data of rocks with a complex internal structure, that is, they often fail to describe the SIP response of rocks.

In addition to mechanistic models, micro-scale numerical simulations can be used to study the SIP response of micro-scale rock models by numerically solving the Nernst-Planck-Poisson (NPP) equations (e.g., Blaschek & Hördt, 2009; Volkmann & Klitzsch, 2010). The NPP equations are a set of coupled partial differential equations describing ion migration and diffusion processes in the electrolyte and along internal interfaces. Micro-scale simulations therefore provide a powerful tool to study structural (e.g., pore space geometry, surface roughness) and electrochemical parameters (e.g., ion mobility, ion charge) that influence the SIP response.

Recently, Bücker et al. (2019) created a numerical model using COMSOL Multiphysics®, a general-purpose finite element simulation software. Bücker et al. (2019) provide two models, a spherical grain used to model the polarization of the EDL and a pore-constriction geometry commonly used to model membrane polarization. Both models, the grain and the pore space have perfectly smooth surfaces represented by spheres and a sequence of cylinders of different diameters, respectively. They validated their numerical results with analytical models (Dukhin et al., 1974; Lesmes & Morgan, 2001; Lyklema et al., 1983). We use their models for EDL polarization around grains and membrane polarization as the basis for our study of the influence of rough surfaces on the SIP response. Our motivation stems from empirical results (Weller et al., 2010) showing a strong correlation between S_{por} and parameters of rock polarization, for example, chargeability m, relaxation time τ, and σ''. With the introduction of surface roughness, we alter S_{por}, and expect therefore changes in the SIP response. Laboratory SIP measurements, for example, on silica beads by Leroy et al. (2008) support this hypothesis. They compared two sets of bead packs with the same bead size, but one set of beads had been treated with an acid to increase the surface roughness. They found an increase of the phase shift and amplitude at higher frequencies (secondary peak) for the rough compared to the smooth beads, which they attributed to the increased surface roughness. In our numerical study, we aim to investigate the influence of surface roughness on the polarization of the EDL around particles.

We have chosen two different approaches to create rough surfaces. First, we add self-similar objects to the surface in a fractal-like fashion. This gives us direct control over structural changes. The second approach is to create a randomly generated surface, which we believe is a suitable method to simulate realistic surface roughness. After simulating the SIP response of models with smooth and rough surfaces, we analyze the influence of surface roughness on the magnitude and frequency dependence of the polarization.

2. Governing Equations

In this section, we present the fundamental theories of the electrical double layer (EDL) and its mathematical description, which we use as the governing equations in our study. First, we describe the EDL at the solid-water interface, which primarily drives the two main polarization processes of non-conducting solid particles in the low frequency range. Then, we introduce the Nernst-Planck-Poisson (NPP) model, which serves as a mathematical characterization of the EDL by considering the coupled ion migration and diffusion processes within an electrolyte and their relation to an electric potential field. We also present the equations derived from the NPP equation
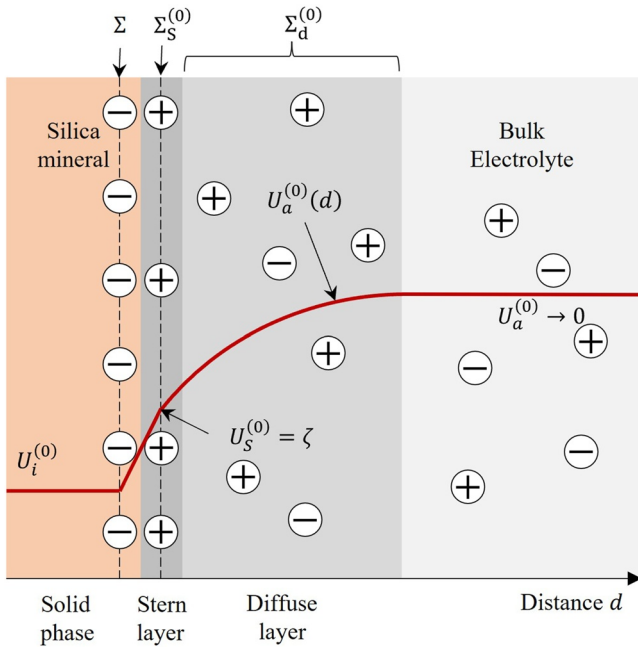
Figure 2. Schematic representation of the electrical double layer on charged silica surface at equilibrium. Deprotonation of silanol surface sites produces a negative surface charge density Σ. This typically negative surface charge is compensated by positive charges distributed over the Stern layer ($\Sigma_S^{(0)}$) and the diffuse layer ($\Sigma_d^{(0)}$). The red line shows the spatial variation of the electric potential $U^{(0)}$ in the different parts of the EDL.

that are used in COMSOL Multiphysics® to study the SIP response of rock models. We conclude this section with a brief description of the methods used to calculate conductivity spectra from the simulation results and their quantitative analysis.

2.1. Electrical Double Layer

In contact with an electrolyte, most rock minerals exhibit a surface charge due to chemical reactions at the electrolyte-mineral interface. The surface charge varies with the pH of the electrolyte and the chemical composition of the mineral phase. We consider silica surfaces in contact with a monovalent electrolyte such as NaCl, where deprotonation of silanol surface sites produces a negative surface charge density Σ over a wide pH range (e.g., Revil & Glover, 1998). Due to Coulomb forces, ions of opposite charge (counterions) are attracted, and ions of the same charge (co-ions) are repelled. As a result, two layers are formed in the electrolyte adjacent to the silica surface: a monolayer of counterions adsorbed to the silica surface by chemical interaction, known as the Stern layer. And a second layer, the diffuse or Gouy-Chapman layer, populated mainly by counterions and a small fraction of co-ions, both following Poisson-Boltzmann statistics (Figure 2).

We adopt a model where the Stern layer is assumed to be an infinitely thin layer of counterions. Within the Stern layer, we assume that counterions can only move tangentially to the surface and partially shield the negative surface charge density $-\Sigma$ by a contribution of the uniform surface charge density $\Sigma_S^{(0)}$ (the superscript (0) denotes quantities in the equilibrium state, that is, without external excitation). In the adjacent diffuse layer, the electrolyte has an excess of counterions due to the remaining attractive forces of the partially shielded surface charge. Within the diffuse layer, ions can move freely without restriction. With d as the distance to the particle surface, the total positive charge density within the diffuse layer $\rho(d)$, after an integration over the diffuse layer thickness, gives the equivalent surface charge density $\Sigma_d^{(0)}$. Together, the Stern and diffuse layers describe the EDL. With increasing distance from the surface, counterions compensate for the negative surface charge $-\Sigma = \Sigma_S^{(0)} + \Sigma_d^{(0)}$, and the electrostatic potential eventually dissipates to zero.

At a characteristic distance from the surface, the electrostatic potential dissipates to $1/e$ (Euler's number), to approximately 1/3, of the initial potential at the solid liquid interface. This characteristic distance is expressed by the Debye length λ_D:

$$\lambda_D = \sqrt{\frac{\varepsilon_0 \varepsilon_a k_B T}{2 N_A e^2 I}} \tag{4}$$

with $\varepsilon_0 = 8.85 \times 10^{-12}$ F/m as vacuum permittivity, and ε_a as the relative permittivity of the electrolyte, $k_B = 1.381 \times 10^{-23}$ J/K as Boltzmann constant, T as absolute temperature, $N_A = 1.602 \times 10^{23}$ mol^{-1} as Avogadro constant, $e = 1.602 \times 10^{-19} C$ as elementary charge, and I as ionic strength of the electrolyte. At the inner boundary of the diffuse layer, the electrostatic potential is typically assumed to be equal to the ζ-potential at the shear plane (e.g., Bücker & Hördt, 2013a; Leroy et al., 2008) and can be computed from the total charge density in the diffuse layer via the Grahame equation (Grahame, 1947)

$$\zeta\left(\Sigma_d^{(0)}\right) = -\frac{2k_B T}{e} \sinh^{-1}\left(\Sigma_d^{(0)} \frac{\kappa}{4 e c_i^{(0)}}\right) \tag{5}$$

with κ as the inverse Debye length, and $c_i^{(0)}$ as bulk ion concentrations.

Helmholtz (1853) presented the first model of the EDL comprising surface charges and a rigid molecular layer of counter-ions with a finite size neutralizing these surface charges. Within this layer, the surface charge potential dissipates linearly with distance from the charged surface. Later, Gouy (1910) and Chapman (1913) postulated their model

of a diffuse layer considering Brownian motion of ions and molecules. Within the diffuse layer, both co-ions and counter-ions can move freely. Furthermore, the local ion density of counter-ions and co-ions, and therefore the surface charge potential, change exponentially with distance from the charged surface according to the Boltzmann equation:

$$c_i(\boldsymbol{r}) = c_i^0 \exp\left(\frac{-ez_i}{k_B T} U_a^{(0)}(\boldsymbol{r}) \right) \tag{6}$$

With c_i as concentration of ion species i, z_i as signed ion valence, and $U_a(\boldsymbol{r})$ electric potential in the electrolyte.

Eventually, Stern (1924) unified both theories in his double layer model. There, the Stern layer is made up of the rigid molecular layer of finite sized counter-ions adsorbed onto the surface. And the adjacent diffuse layer, comprises the point charges of co- and counter-ions. The electrostatic potential within the EDL partially dissipates in the Stern layer in linear fashion with distance from the solid-liquid interface. In the diffuse layer, this partially compensated potential further decays exponentially due to the ion density following the Boltzmann equation.

2.2. The Nernst-Planck-Poisson Equation System

The Nernst-Planck-Poisson (NPP) equations are a coupled system of partial differential equations. They describe the spatial and temporal variation of ion concentrations $c_i(\boldsymbol{r},t)$ of ion species i and electric potential $U(\boldsymbol{r},t)$ in an electrolyte due to concentration and electric potential gradients and convective flow. The Poisson equation resembles the coupling term in that it relates the electric field strength to charge density distributions, that is, ion concentrations. Together, these equations form the mathematical basis for a quantitative description of all processes involving ion migration and diffusion in electrolytes with and without the presence of external electric fields. We do not consider convective flow in our models and omit the corresponding part of the Nernst-Plank equation. For the sake of readability, we will write φ for $\varphi(\boldsymbol{r},t)$ and c_i for $c_i(\boldsymbol{r},t)$ in the following paragraphs.

First, we look at Poisson's equation, starting with Gauss' law in differential form as

$$\nabla \cdot \boldsymbol{D} = \rho \tag{7}$$

where $\nabla\cdot$ is the divergence operator, $\boldsymbol{D}$ is the electric displacement field, and ρ_f is the free charge volume density. In a homogeneous, isotropic, non-dispersive, linear medium the relationship between the electric displacement field and the electric field $\boldsymbol{E}$ is given by

$$\boldsymbol{D} = \varepsilon_0 \varepsilon_r \boldsymbol{E} \tag{8}$$

Substituting (8) into Gauss' law (7), and assuming a spatially constant relative permittivity ε_r we obtain

$$\nabla \cdot \boldsymbol{E} = \frac{\rho}{\varepsilon_0 \varepsilon_r} \tag{9}$$

where ρ is the total volume charge density. If we further assume, that there is no magnetic field, we can describe the electric field E as the gradient of the scalar electric potential U:

$$\boldsymbol{E} = -\nabla U \tag{10}$$

Substituting the potential gradient for the electric field in Equation 9 gives Poisson's equation for electrostatics:

$$\nabla^2 U = -\frac{\rho}{\varepsilon_0 \varepsilon_r} \tag{11}$$

Finally, we can replace ρ with $F \sum_i z_i c_i$, where F is the Faraday constant, to obtain the Poisson-Boltzmann equation:

$$\nabla^2 U = -\frac{F}{\varepsilon_0 \varepsilon_r} \sum_i z_i c_i \tag{12}$$

Solving Equation 11 for the potential requires information about the ion concentrations c_i. We can obtain this information by solving the Nernst-Planck equation.

The Nernst-Planck equations describe the total flux of ionic species in an electrolyte. In our studies, we use a binary electrolyte as the fluid medium. For simplicity, we also assume that the mobilities of cations (index p) and

anions (index n) are equal. Ion mobilities μ_i of ion species i relate ion drift velocities to the applied electric force. The ion mobility is related to the diffusion coefficient D by the Einstein relation $D = \mu k_B T / e$.

When dissolved in water, a binary electrolyte such as NaCl dissociates into cations (positive ions) and anions (negative ions) that are uniformly distributed throughout the volume. The total flux $\boldsymbol{J}$ of ion species i, in the absence of advective mass flow, is given by:

$$\boldsymbol{J}_i = -D_i \nabla c_i + \mu_i c_i z_i \boldsymbol{E} \tag{13}$$

The first term represents the diffusive flux due to an ion concentration gradient ∇c_i with diffusion coefficient D_i. The second term represents the electro-migratory flux due to an external electric field $\boldsymbol{E}$. The ionic charges are expressed by the elementary charge e and their respective valence z_i. Using Equation 10 we can also write:

$$\boldsymbol{J}_i = -D_i \nabla c_i - \mu_i c_i z_i \nabla \mathrm{U} \tag{14}$$

Furthermore, following the conservation of electric charge with the continuity equation

$$\frac{\partial c_i}{\partial t} = -\nabla \cdot \boldsymbol{J}_i \tag{15}$$

where t is time. Combining Equations 14 and 15 gives the Nernst-Planck equation:

$$\frac{\partial c_i}{\partial t} = \nabla \cdot (D_i \nabla c_i + \mu_i c_i z_i \nabla \mathrm{U}) \tag{16}$$

For an external harmonic excitation $\boldsymbol{E} = \boldsymbol{E}_0 exp(j\omega t)$, where $\boldsymbol{E}_0$ is the strength of the external electric field, $j = \sqrt{-1}$, and ω is the angular frequency, we can express the electric potential and ion concentrations as the sum of a static equilibrium and a perturbation part (Bücker et al., 2019):

$$U(r,t) = U^{(0)}(\boldsymbol{r}) + \delta U(\boldsymbol{r}, \omega) \cdot \exp(j\omega t) \tag{17}$$

$$c_i(r,t) = c_i^{(0)}(\boldsymbol{r}) + \delta c_i(\boldsymbol{r}, \omega) \cdot \exp(j\omega t) \tag{18}$$

By substituting Equations 17 and 18 into Equations 12 and 16 and performing a Fourier-transform on the resulting system, the problem can be divided into a static part and a frequency-dependent part. The static part can be solved independently, while the frequency-dependent part is coupled to the static solution (Bücker et al., 2019).

3. Methods

In this paper, we numerically solve the Fourier transform of Equations 12 and 16 to study the frequency-dependent electrical properties of rock models. We perform our studies following the workflow published by Bücker et al. (2019). They used COMSOL Multiphysics®, a finite element simulation software, to solve the coupled system of partial differential equations described below. The mathematical model is based on Equations 16 and 17, which are divided into two steps: a steady-state solution and a frequency-dependent solution of the NPP equations. Bücker et al. (2019) based their mathematical model on the publications of Chew and Sen; Chew and Sen (1982a, 1982b). In the following section, we will briefly describe the implementation of the mathematical and physical model in COMSOL Multiphysics.

For the stationary solution of Equation 17, where no external electric field is applied to the model, the potential distribution can be derived by solving the Poisson-Boltzmann equation

$$\nabla^2 U^{(0)}(\boldsymbol{r}) = -2c_0 \frac{F}{\varepsilon_0 \varepsilon_r} \sinh\left(\frac{U^{(0)}(\boldsymbol{r})}{k_B T}\right) \tag{19}$$

where c_0 is the bulk electrolyte concentration. The ion concentrations do not require additional numerical calculations as they are linked to the potential via the Boltzmann Equation 6.

In the second step of the simulation, we perform a parametric sweep over the model parameter ω (angular frequency) to simulate frequency dependent behavior, obtaining solutions for a discretized range of angular frequencies. We compute the potential perturbation within the electrolyte domain as well as the cation (c_p) and anion (c_n) perturbations by solving the following system of equations

Table 1
Parameter List of Our Modeled Electrolyte

Parameter	Unit	Value
Bulk ion concentration, $c_{p,n}^{(0)}$	mol/m^3	1
Bulk ion mobility, $\mu = \mu_p = \mu_n$	m^2/(Vs)	5E−8
Ion mobility in Stern layer, μ_S	m^2/(Vs)	5E−9
Relative fluid permittivity, ε_a	–	80
Temperature, T	K	293
External field strength, E_0	V/m	1
Fraction of charge in Stern layer, p	–	0.5

$$\nabla \cdot \left[-\begin{pmatrix} D & 0 & -\mu c_0 \exp\left(\frac{U}{k_B T}\right) \\ 0 & D & \mu c_0 \exp\left(\frac{U}{k_B T}\right) \\ 0 & 0 & \varepsilon_0 \varepsilon_r \end{pmatrix} \cdot \nabla \begin{pmatrix} c_n \\ c_p \\ U \end{pmatrix} - \begin{pmatrix} -\mu \nabla U & 0 & 0 \\ 0 & \mu \nabla U & 0 \\ 0 & 0 & 0 \end{pmatrix} \begin{pmatrix} c_n \\ c_p \\ U \end{pmatrix} \right]$$

$$+ \begin{pmatrix} j\omega & 0 & 0 \\ 0 & j\omega & 0 \\ F & -F & 0 \end{pmatrix} \begin{pmatrix} c_n \\ c_p \\ U \end{pmatrix} = 0 \qquad (20)$$

Equation 20 includes the Fourier transformed Equations 12 and 16 formulated in the frequency domain for the perturbations only. In addition, we solve for the perturbation of the potential U_S at the solid-electrolyte interface (Bücker et al., 2019):

$$\nabla_S \left(-D_S \nabla_S \delta\Sigma_S - \mu_S \Sigma_S^{(0)} \nabla_S U_S \right) + i\omega U_S = 0 \qquad (21)$$

where ∇_S denotes differential operators acting along the particle surface and $\Sigma_S(\boldsymbol{r}, t) = \Sigma_S^{(0)}(\boldsymbol{r}) + \delta\Sigma_S(\boldsymbol{r}, \omega) \cdot \exp(j\omega t)$ denotes the surface-charge density in the Stern layer. Since the potential at the surface is assumed to be continuous, $U = U_S$ at all points along the particle surface.

For a thorough description of the underlying mathematical framework, we refer to Bücker et al. (2019).

3.1. Models

Here we introduce our models; first, the general model geometry. We then explain how we modify our models to mimic the roughness of the inner rock surface (Sections 3.1.1 and 3.1.2), followed by model parametrization (Section 3.1.3). Finally, we describe post-processing steps, including the calculation of the frequency-dependent conductivity from the simulation results (Section 3.2). Regarding the model geometries, we use the spherical (grain) models of Bücker et al. (2019). Apart from introducing surface roughness and adjusting the size of the finite element mesh, we have refrained from modifying the authors' simulation workflow and model design. In the discussion section, we will highlight advantages and shortcomings of the provided implementation for our specific case.

We consider a cylindrical domain with a spherical particle at the center of the cylinder. The cylindrical domain has the properties of a liquid electrolyte with commonly used parameters (Table 1). To ensure a constant volumetric particle content of our models throughout all studies, we coupled the domain volume to the particle volume. Furthermore, we sized the domain appropriately to avoid the influence of boundary conditions on the calculations at the electrolyte-particle interface. For a particle radius of $r_p = 5$ μm, we set the cylinder height and diameter to $h_c = d_c = 40 \cdot r_p$. The particle represents a solid, non-conducting grain with either a smooth or rough, electrically charged surface. Thus, our models represent dilute suspensions of such particles.
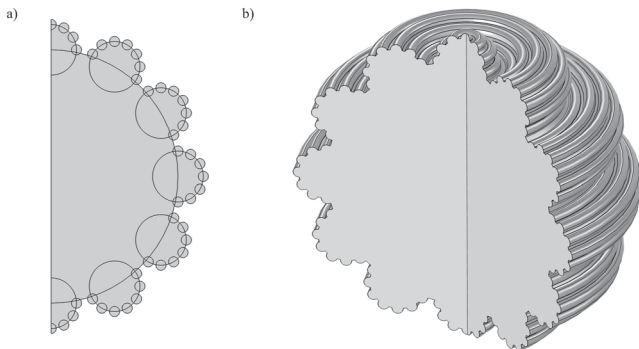
We create our models in COMSOL's 2D axisymmetric space dimension, a special environment for axisymmetric 3D geometries, like in our case. It is a common strategy to significantly reduce computational memory and time by taking advantage of model symmetry. In this case, we build our model in a 2D plane $(\boldsymbol{r}, \boldsymbol{z})$ of a cylindrical coordinate system (Figure 3a). Before solving a 2D problem in the *rz*-plane, all coefficients must be multiplied by the radial coordinate $\boldsymbol{r}$ to describe the rotational symmetry of the problem. Since we are exploiting axis symmetry in 3D, the resulting particles resemble objects that have been formed on a turning lathe (e.g., Figure 3b). Surely, real surface roughness would not look like this. We will address the implications of this characteristic structure in our discussion.

Figure 3. Self-similar grain model with two daughter generations. (a) Geometrical assembly of the grain within the 2D axisymmetric plane. (b) Resulting 3D geometry.

3.1.1. Self-Similar Geometries

To increase the surface area of our grain models, we implement a finite, semi-fractal geometry by placing smaller daughter grains on the surface of a

Table 2
Grain Radii of Fractal Models

	Grain radius		
	Group A		Group B
	[m^{-6}]		
1st generation, r_p	20		5
2nd generation, $r_{d,1}$	4		1
3rd generation, $r_{d,2}$	0.8		0.2

parent grain. In 2D, this corresponds to circles with their centers positioned on the contour of the parent circle (Figure 3a). The primordial particle has a radius of $r_p = 20$ or 5 µm. The radii of the first and second daughter generations ($r_{d,1}$ and $r_{d,2}$) are each five times smaller than the previous generation (Table 2).

3.1.2. Randomly Generated Surfaces

Following an approach by Sjodin (2017), we use harmonic functions in conjunction with random number generators to resemble natural rough surfaces (Figure 4). We generate these surfaces in the 2D rz-plane by using a sum of trigonometric functions, like in a Fourier series:

$$\begin{pmatrix} r(s) \\ z(s) \end{pmatrix} = r_p \begin{pmatrix} \sin(s) \\ \cos(s) \end{pmatrix} \left[1 + a \sum_{k=-N}^{N} \left(k^2 \right)^{-\frac{b}{2}} g(k) \cos(2\pi k s + u(k)) \right] \quad (22)$$

where a is the maximum amplitude, $k = 2\pi/\lambda$ is the wavenumber or spatial frequency and λ is the wavelength, b is the attenuation exponent, s is the spatial variable along the surface with $0 = s \leq \pi \cdot r_p$, $g(k)$ is a random function, which creates random numbers from a normal distribution, and $u(k)$ is a random function with uniform distribution. The left term on the right-hand side of Equation 22 creates a half circle with the radius r_p. The sum term on the right creates the random roughness along the line of the half circle. Each term in this sum represents an elementary wave with a certain wavelength $\lambda = 2\pi/k$. The rough surface is generated by the superposition of N elementary waves with Gaussian distributed amplitudes and uniformly distributed phase angles. The coefficient a determines the maximum amplitude as a function of particle size. In a preliminary study, we determined a scaling factor of $a = 0.1 \cdot r_p$ as a reasonable maximum. For low attenuation exponents $b \leq 1.2$, higher maximum amplitudes resulted in unrealistic surfaces. Reducing the maximum amplitude below a certain threshold had a similar effect as increasing the attenuation exponent b. This exponent accounts for natural processes such as wear and erosion by damping higher frequencies. Consequently, low frequencies will have larger amplitudes than high frequencies, as observed in nature. The normal distribution function $g(k)$ has a mean of $\mu = 0$ and a standard deviation of $\sigma = 1$. The phase angles are sampled from a uniform distribution function $u(k)$ between $-\pi/2$ and $\pi/2$. Summing the wavenumber k over $-N$ to N with equal probabilities ensures the generation of a synthesized surface without a preferred oscillation direction (Sjodin, 2017). Consequently, the maximum amplitude a, the wave count N and the attenuation exponent b are controlling parameters for the generation of rough surfaces. Surface roughness is controlled by b, which takes values between 2 (low roughness) and 1 (high roughness). N controls the spatial frequency content of the surface topography. The difference between high and low values of N is best observed at low values of b, that is, rough surfaces. Low values ($N < 20$) produce smooth, wavy surfaces, while higher values ($N > 20$) produce sharp-edged surfaces.

Please refer to the supporting material of this publication for the complete mathematical parameterization of the surface function in Comsol.

We investigate the influence of randomly generated rough surfaces on the IP response. We modify the surface of two different spheres with radii of 5 and 20 µm. We use different ranges of wavenumbers $k = \{-N,…,N\}$ and vary the attenuation exponent b between 1 (rough) and 2 (smooth) for each range. For high wave counts ($N > 100$), the low-end of b had to be raised to $b = 1.1$. High wavenumbers create sharp surface structures that cannot be resolved with the applied mesh settings without further refinement of the mesh size.

3.1.3. Etched Surfaces

In addition, we have created random surface roughness models where we can choose the preferred direction of oscillation of the trigonometric function, that is, surface roughness is created by either adding or removing material from a smooth particle surface. Removal of material from the surface can be
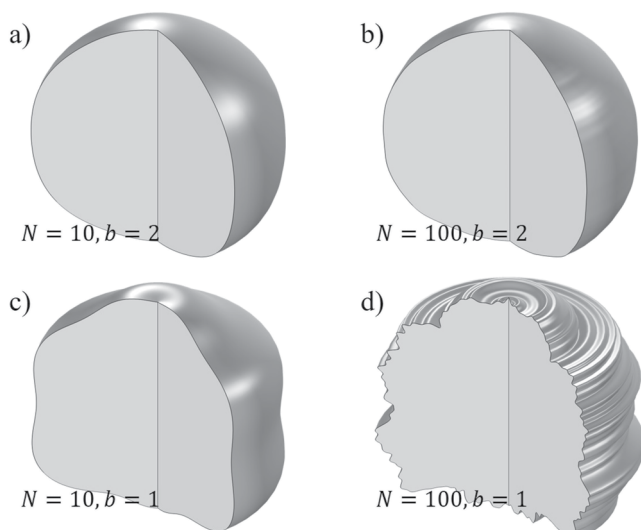
a) $N = 10, b = 2$

b) $N = 100, b = 2$

c) $N = 10, b = 1$

d) $N = 100, b = 1$

Figure 4. 3D models of spherical grains with randomly generated surfaces for different spatial frequencies N and attenuation exponents (b) For $b = 2$ the surface is smooth regardless of the spatial frequency content (a) $N = 10$, and (b) $N = 100$. For $b = 1$, we see (c) undulating surfaces with $N = 10$, and (d) edgy surfaces with $N = 100$.

associated with surface etching or dissolution, while addition of material can be associated with processes such as precipitation, flocculation, or bacterial growth.

To create the etched surfaces, we used the same method as for the randomly generated surfaces. To control the direction of oscillation, we used an if condition in the surface parameterization in Comsol, which sets all positive values of the surface function to zero. We also included a second condition that allows us to filter out low wavenumbers, that is, $k < 10$, to avoid the longer wavelengths of the spatial oscillation. These lower wavelengths produce smooth, dent-like structures on the surfaces, which in our opinion do not resemble an etched surface as seen in Leroy et al. (2008).

3.1.4. Model Parametrization and Boundary Conditions

Our models consist of a solid phase (particle) and a liquid phase (electrolyte), each with its own set of physical properties (Table 1). In addition, we assign boundary conditions to the outer and inner boundaries, that is, the solid-fluid interface, before solving the NPP equations. The partition coefficient p (Bücker et al., 2019) defines the fraction of the surface charge that is compensated by the Stern layer (see Section 2.1)

$$p = \frac{-\Sigma_S^{(0)}}{\Sigma} \tag{23}$$

For $p = 0$, there are no counter ions in the Stern layer and the surface charge is compensated only by charges in the diffuse layer. At $p = 1$, the surface charge would be compensated only by counterions in the Stern layer. At $p = 0.5$, the counterions are equally distributed between the Stern and diffuse layers and equalize the surface charge.

The two simulation steps, the steady-state solution and the frequency-dependent solution of the NPP equations, require different boundary conditions. For the steady-state problem, we set a zero potential at the outer domain boundaries and assume a fixed surface charge density $\Sigma = -0.01$ C/m² at the solid-electrolyte interface. For the frequency-dependent solution, we apply an electric field of 1 V/m parallel to the symmetry axis of our model domain. We assign potentials of $U = \pm E_0 L$ at the bottom and top of the cylindrical fluid domain, where L is half the length of the cylindrical domain. Further, we assign a zero-flux condition to the cylinder wall. The perturbation of the ion concentrations at these boundaries is set to zero, that is, equal to the equilibrium bulk concentration.

Regarding the discretization of our models, we use two different meshing options, following the approach of Bücker et al. (2019). We reduce the size of the mesh elements at the charged surface to allow the resolution of the processes inside the electrical double layer. To do this, we use COMSOL's built-in boundary layers. Eight boundary layer elements extend perpendicularly on each side of a charged surface. The minimum height of these cells is set to half a Debye length and increases by a factor of 1.2 outward. In the direction parallel to the surface these elements are segmented with a minimum size of 5×10^{-3} r_p. In the adjacent fluid and solid domains, the triangular mesh is used, increasing by a factor of 1.25 toward the outer boundaries to a maximum element size of $1/20L$.

3.2. Model Conductivity Calculation and Analysis

If the applied electric field is parallel to the electric current passing through the electrolyte domain, which is the case in our models, an approximation for the current density can be expressed as the product of the electric conductivity and the electric field strength $J = \sigma E$. In our models, this corresponds to the product of the observed electric field E_{obs} and the complex electrolyte conductivity $\sigma_a^*(\omega) = \sigma_a + j\omega\epsilon_0\epsilon_a$ or, alternatively, the product of the external electric field E_0 and the effective complex conductivity $\sigma_{eff}^*(\omega)$ (Bücker et al., 2019):

$$E_{obs}\sigma_a^* = E_0\sigma_{eff}^* \tag{24}$$

Consequently, We can write

$$\frac{\sigma_{eff}^*}{\sigma_a^*} = \frac{E_{obs}}{E_0} = \sigma_{sim}^* \tag{25}$$

Using Equation 25, we define the simulated complex conductivity as the effective complex conductivity normalized by the fluid conductivity. We obtain the complex conductivity of our models by numerically integrating the total ion flux densities over the cross-section of our domain at the top or bottom of the cylinder:

$$\sigma_{sim}^* = \frac{2F}{E_0 R_0^2} \int_0^{R_0} [\boldsymbol{J}_+(r) + \boldsymbol{J}_-(r)]e_z r \, dr \tag{26}$$

This integration gives us the effective complex conductivity normalized by the complex fluid conductivity. The factor $2/R_0^2$ accounts for the normalization with the cross-sectional area with $R_0 = d_c/2$ (see Section 3.1) as the radius of the cylindrical domain and the term rdr accounts for the area element of the boundary.

Throughout our study, we have ensured that the solid volume fraction $\nu_{mod} = V_p/V$, where V_p is the particle volume, and V is the total volume of the model domain, remains constant for all models. For smooth spherical grains this is simply done by linking the domain size to the grain radius. For more complex geometries, we determined the grain volume numerically and calculated an equivalent radius for a smooth sphere. Using this equivalent radius, we adjusted the domain size to match our desired volume ratio. Following the approach of Bücker et al. (2019), we adjust the volumetric solid fraction of our model ν_{mod} to that of a suspension of the modeled grain $\nu_{sus} = 0.4$. The procedure is derived from the Maxwell-Wagner mixing rule according to the formula:

$$f(\omega) = \frac{1}{\nu_{mod}} \frac{\sigma^*_{mod}(\omega) - \sigma^*_a(\omega)}{\sigma^*_{mod}(\omega) + 2\sigma^*_a(\omega)} \tag{27}$$

where $f(\omega)$ is the reflection coefficient. With the reflection coefficient we can calculate the upscaled conductivity with the desired $\nu_{sus} = 0.4$:

$$\sigma^*_{sus}(\omega) = \frac{1 + 2\nu_{sus}f(\omega)}{1 - \nu_{sus}f(\omega)} \tag{28}$$

With COMSOL Multiphysics® we calculate the surface area of the modeled particle S_{mod}, the particle volume V_p, and the total model volume V. After upscaling of the volumetric particle content from ν_{mod} to ν_{sus}, we calculate S_{por}. We keep the total volume V constant and treat the upscaling process as an increase in particle number. Thus, the mineral surface area increases by a factor of $\nu_{sus}/\nu_{mod} = 600$. We can then calculate the specific surface area per unit volume (S_{tot}), which is the mineral surface area $S = 600S_{mod}$ normalized by the total volume V:

$$S_{tot} = 600\, S_{mod}/V \tag{29}$$

After calculation of S_{tot}, we obtain

$$S_{por} = \frac{S_{tot}}{\phi} = \frac{S_{tot}}{1 - \nu_{sus}} \tag{30}$$

For the quantitative analysis of our simulation data, we use the Debye decomposition (DD) method (Nordsiek & Weller, 2008), which is effective for analyzing SIP data regardless of the shape of the conductivity spectra. The DD fits the polarization magnitudes m_j to a defined range of discrete time constants τ_j over the measured frequency range ω of the SIP response spectra. The fitted complex conductivity is defined by:

$$\sigma^*(\omega) = \sigma_0 / \left(1 - \sum_{j=1}^{n} m_j \cdot \left(1 - \frac{1}{1 + i\omega\tau_j} \right) \right) \tag{31}$$

The result is a distribution of Debye relaxations characterized by the polarization magnitudes m_j. Summing up the polarization magnitudes m_j gives the total polarization m_t:

$$m_t = \sum m_j \tag{32}$$

To avoid the influence of Maxwell-Wagner polarization, we fit our data in the frequency range between $10^{-1}-10^5$ rad/s. We then multiply the calculated total chargeability by the dc conductivity σ_0 to obtain the normalized chargeability m_n:

$$m_n = m_t\sigma_0 \tag{33}$$

4. Results

In this section, we show the simulated frequency-dependent conductivity of our models. Here, we omit the plots of $\sigma'(\omega)$ and only show plots of $\sigma''(\omega)$, which we think is a more suitable way to display the polarization.
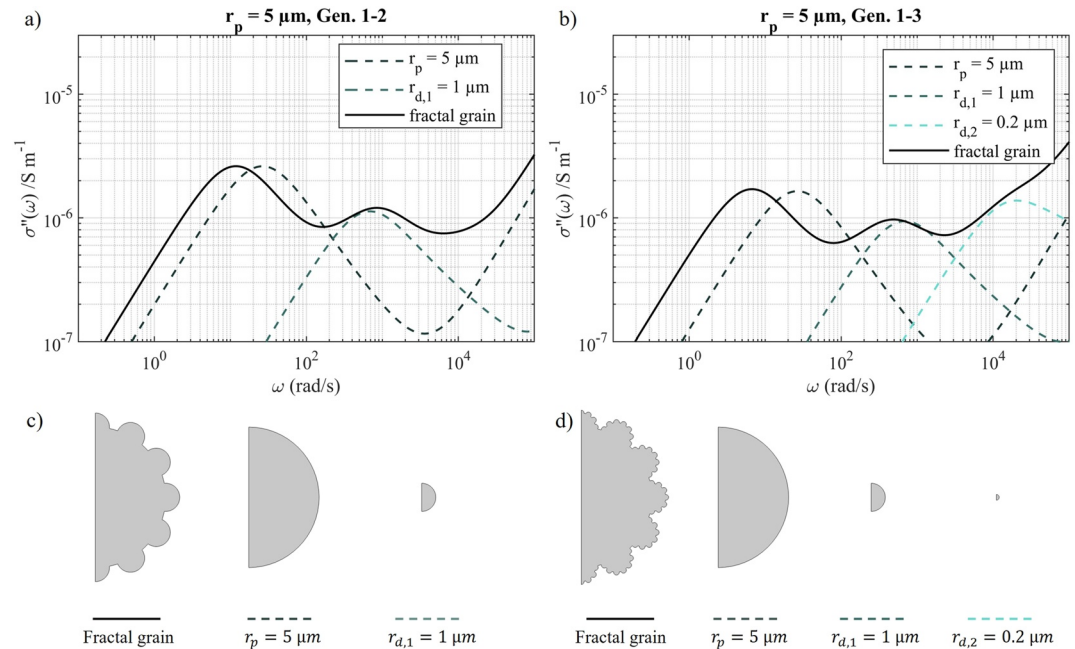
Figure 5. Imaginary conductivity of fractal grain models with (a) one and (b) two additional daughter generations. The solid lines represent the fractal models, the other lines are spectra of smooth models used to construct the fractal models. (c) 2D axisymmetric sketch of the particle for the fractal grain with one daughter generation and the smooth particles. (d) 2D axisymmetric sketch of the particle for the fractal grain with two daughter generations and the smooth particles.

4.1. Fractal Models

Figure 5 shows the SIP response of fractal grain models with one and two daughter generations compared to the spectra of the smooth particles that make up the fractal model. The original particle has a radius of $r_p = 5$ μm and the radii of the two daughter generations are $r_{d,1} = 1$ μm and $r_{d,2} = 0.2$ μm. The polarization magnitudes of the smooth particles were adjusted to match their respective magnitude in the fractal model to emphasize the peak shifts. The unmodified response spectra can be found in the supporting material for this publication.

Figure 5a shows the effects of one daughter generation. The primary peak shifts from around 20–30 rad/s for the smooth particle to 10 rad/s. The secondary peak caused by the daughter generations shifts from around 70 rad/s for the smooth particle to 90 rad/s in the fractal model. The magnitude decreases by 44% (not visible in Figure, because magnitudes are scaled). With the addition of the second daughter generation to the grain surface (Figure 5b), we observe additional polarization at $\omega = 10^4$ rad/s and a shift in the position and magnitude of all polarization peaks with respect to signals of the smooth models. The primary peak at 10 rad/s shifts further toward lower frequencies. This is now also true for the secondary peak at about 10^3 rad/s (Figure 4b). Although not visible in 5b, we register a shift of the last polarization peak, caused by the latest daughter generation, to slightly higher frequencies. In comparison to the fractal model with one daughter generation, the magnitude of the primary polarization decreases by 79% from around $3.9 \cdot 10^{-6}$ S/m (see Supporting Information S1) to $1.8 \cdot 10^{-6}$ S/m.

4.2. Random Surface Geometries

Figure 6a shows the imaginary conductivity of the simulations with a fixed wave count $N = 50$ and an attenuation exponent b varying between 1 (rough surface) and 2 (smooth surface). We added the response of the fractal model for comparison. The spectra show a dominant contribution of the grain size ($r_p = 5$ μm) in the frequency range between 10–30 rad/s. With decreasing spectral exponent b, that is, increasing roughness, a slight shift of the primary peak toward lower frequencies and slightly lower magnitudes can be observed. Furthermore, a polarization in the frequency range between 10^2–10^4 rad/s develops, which is expressed by an increase of the imaginary part within this interval. Compared to the spectra of the fractal models, the primary peak shift and the secondary polarization are less pronounced. This is mainly due to the relatively large size of the daughter generations ($r_d = 0.2 \cdot r_p$) compared to the maximum amplitude of the trigonometric surface function ($a = 0.1 \cdot r_g$).
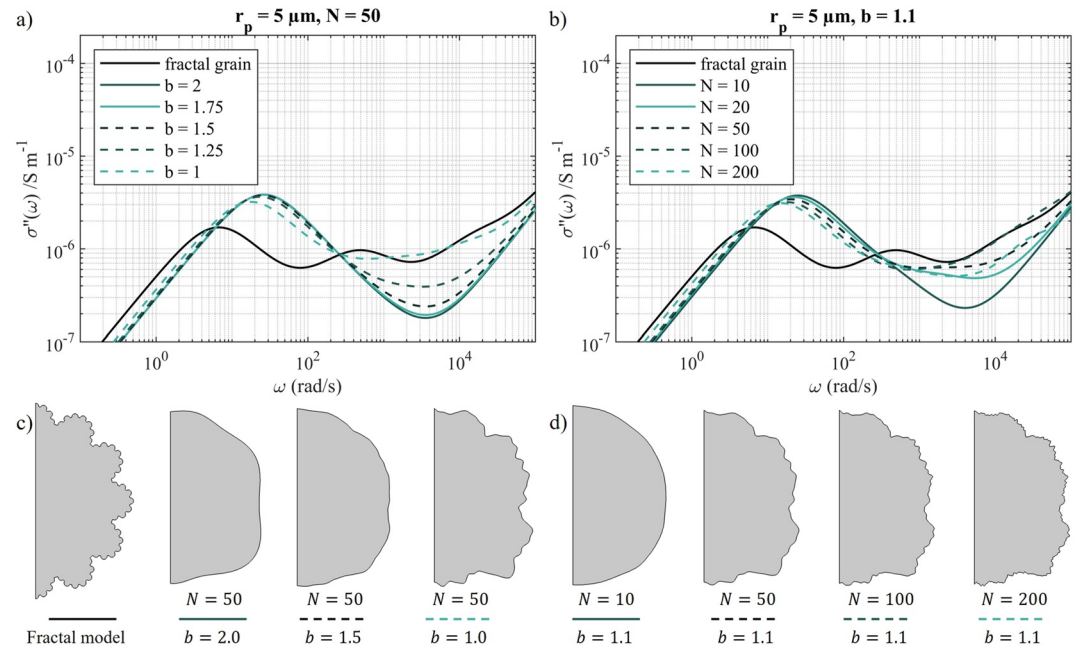
Figure 6. Imaginary conductivity spectra of spheres with randomly generated rough surfaces. (a) shows the effects of a varying attenuation exponent b and (b) of a varying spatial frequency content N. Sketches of the particle surface of (c) the fractal model and the random model with three stages of varying attenuation exponent, and (d) the four random models with varying wave count N.

Figure 6b shows the results of simulations with different wave counts $N = \{10, 20, 100, 200\}$ for a fixed attenuation exponent $b = 1.1$. Again, we observe a dominant contribution of the grain diameter and slight shifts in the position and magnitude of the primary peak. Furthermore, we observe a pronounced effect of the surface roughness, which is expressed by an increased polarization in the range of about 10^2–10^4 rad/s for $N \geq 20$. For wave counts $N < 100$ and attenuation exponents $1.5 < b < 2$, we observe slight changes in the primary peak and slightly increased polarization at frequencies above the primary peak frequency. For higher wave counts $N \geq 100$ and low attenuation exponents $b < 1.25$, we see a stronger influence on the primary peak and an increase in polarization above the primary peak frequency.

4.3. Etched Surface Geometries

SIP responses from models where we have removed material from the smooth surface generally show similar behavior. We also observe a shift in the primary polarization frequency and magnitude as well as the formation of secondary polarizations.

Figure 7 shows the results of our studies with a preferred direction of oscillation of the surface structures. First, we illustrate the difference between adding and removing material on an exaggerated model. We chose a single harmonic function with the wavenumber $k = 12$ and an amplitude of $a = 0.2r_p$. We observe similar behavior with respect to the primary polarization shift and the build-up of a secondary polarization. Figure 7b shows the effect of surface etching, that is, removal of surface material. The model with the highest wavenumber count ($N = 200$) has the greatest effect on the SIP response. The models with the lower wavenumber count ($N = 20$) show only small secondary polarizations as increased imaginary conductivity in the range of 10^3–10^4 rad/s. We see that increasing the maximum amplitude of the surface generator function for the $N = 20$ model from $a = 0.1$ to $a = 0.2$ has only a small effect on the SIP response, slightly increasing the secondary polarization.

Our results reveal two main aspects of surface roughness: a shift of the primary polarization peak, and the generation of secondary polarization. In order to see how our results compare to laboratory measurements and analytical models, we have performed an extensive analysis, which we present in the following discussion section.
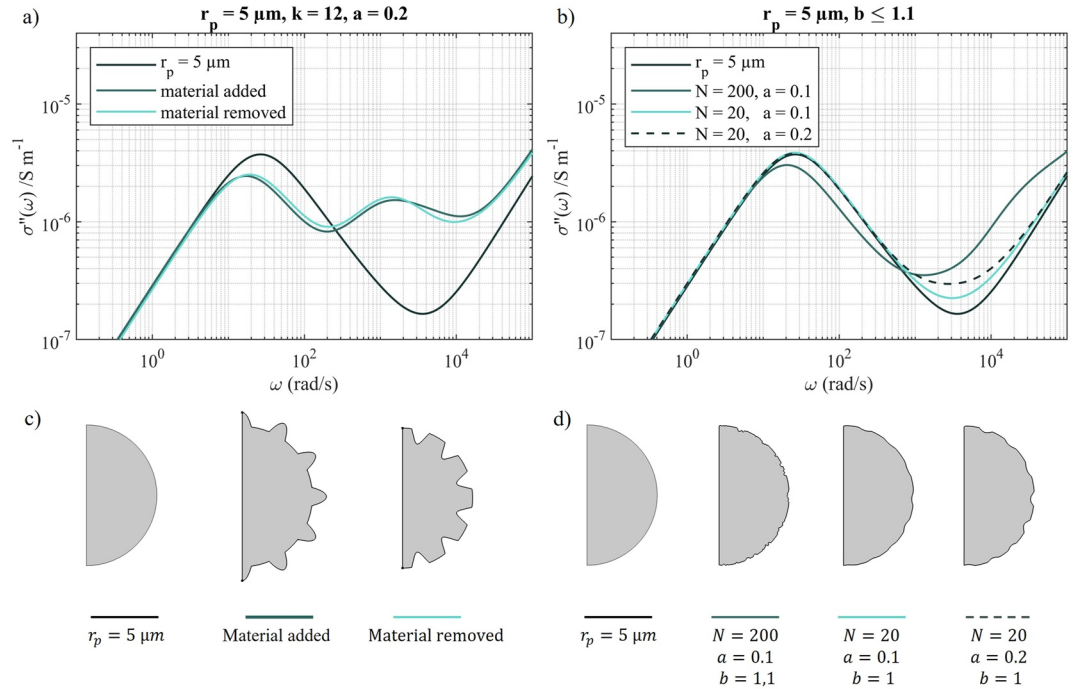
Figure 7. Imaginary conductivity spectra of surfaces with a preferred direction of oscillation. (a) Comparison of removing and adding material to the surface with a single harmonic function. (b) Surface etching (removal of material) with the random surface function (Equation 22). (c and d) illustrate the corresponding surface geometries depicted in the conductivity spectra.

5. Discussion

In the previous section, we presented exemplary results of our simulations, that is, imaginary conductivity spectra of the studied grain models with fractal and randomly generated surfaces. We observe distinct changes in the spectral behavior of grains with rough compared to smooth surfaces. Compared to the smooth grain, the primary peak is slightly shifted to lower frequencies for both rough surface types. In contrast to the fractal models, which show an additional peak for each daughter generation, the randomly generated surface models create secondary polarizations over a wide range of frequencies, but mostly no distinct polarization peaks.

To further evaluate the influence of surface roughness, we now compare the SIP parameter determined by Debye decomposition of all simulated spectra with empirical results from SIP measurements on rock samples as well as with responses from mechanistic EDL polarization models. We discuss the influence of surface roughness on the frequency dependence and on the polarization strength.

5.1. Influence of Surface Roughness on Frequency Dependence

Figures 8a and 8b show the relaxation time over the grain radius for all the models studied (symbols). In the case of rough grains, we chose the relaxation time of the first peak as it reflects the grain size. We have added plots of an analytical model for the relaxation time as a function of grain size:

$$\tau = r^2/2D_S M \tag{34}$$

with grain radius r, Stern layer diffusion coefficient $D_S = 1.3 \times 10^{-10}\ m^2/s$, and coupling coefficient M (Lyklema et al., 1983). The coupling coefficient takes into account the coupling of the charges in the Stern layer to the electrolyte and is defined by:

$$M = 1 + \frac{\kappa \Sigma_S^{(0)}}{2ec_0 \cosh\left[e\zeta/(2k_B T)\right]} \tag{35}$$

where κ is the inverse Debye length. The solid lines in Figures 8a and 8b represent the relaxation time with charges equally distributed between Stern and diffuse layers ($p = 0.5, M > 1$). Smooth grains (circles) with
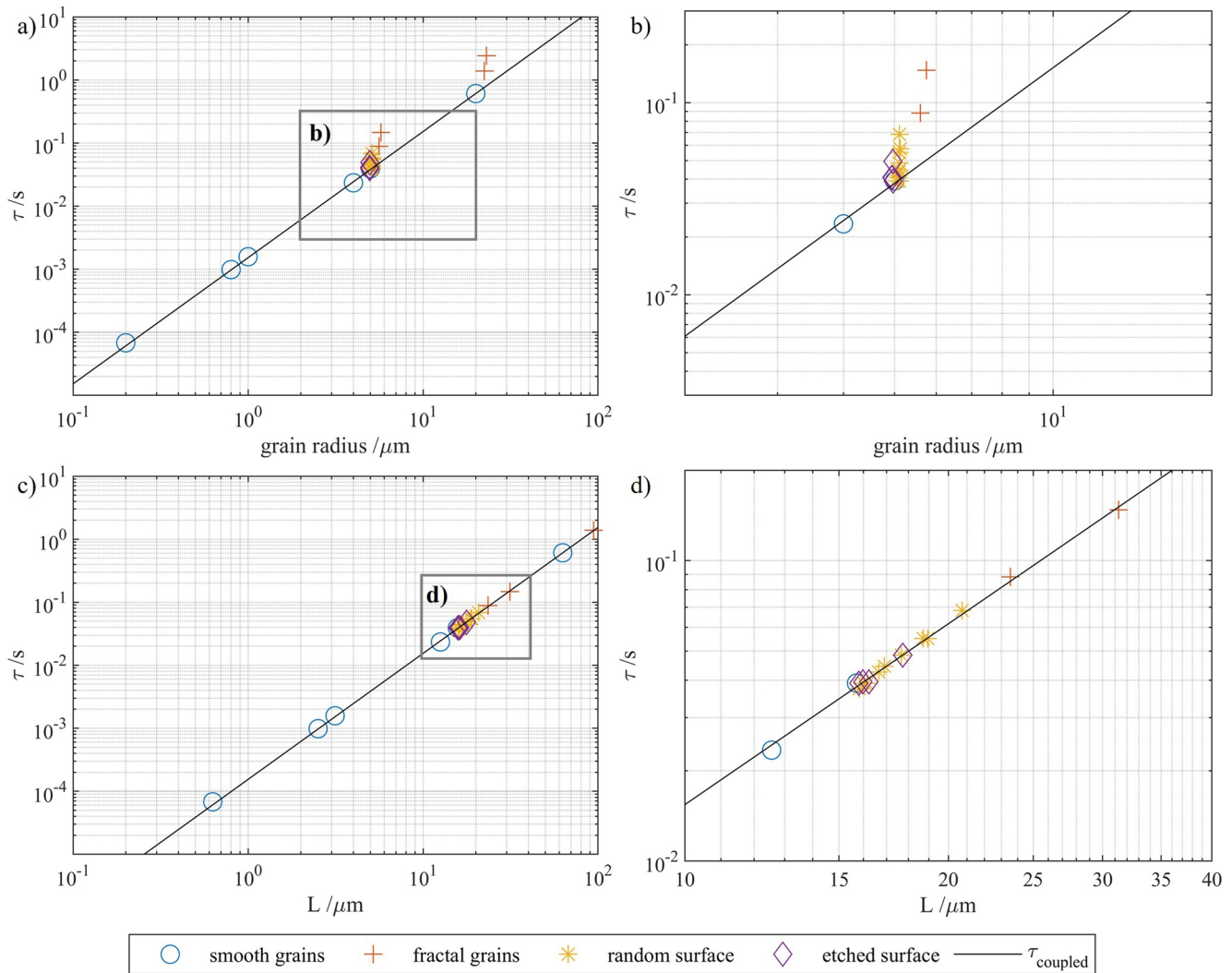
Figure 8. (a) Relaxation time τ versus grain radius. The line shows the prediction of the analytical model for electrical double layer (EDL) polarization (Equation 34). (b) Detail view of the models based on a 5 µm grain radius. (c) Relaxation time τ versus equivalent pore radius L. The line shows the prediction of the analytical model for EDL polarization (Equation 36). (d) Detail view of the models based on a 5 µm grain radius.

$r \geq 4$ µm plot on the solid line. However, grains with rough surfaces have slightly longer relaxation times than grains with smooth surfaces (Figure 8b). This observation is consistent with the shift of the first polarization peak of rough models to lower relaxation frequencies compared to smooth grains of similar size, as seen in Figures 5–7. We attribute this to the increased relaxation path caused by surface roughness, that is, to the longer path along the rough surface compared to the smooth surface that the ions in the EDL traverse to build up or decay the polarization. This interpretation is also consistent with the larger peak shifts observed for grains with high surface roughness than for grains with low surface roughness.

We expect the primary relaxation time of a rough grain to be proportional to the polarization length, the length of the path along the surface connecting the two opposite poles of the polarized grain, which is in our case equal to the circumference of a (rough) hemisphere. In Figures 8c and 8d, we test the hypothesis by plotting the primary relaxation time versus the radius L of a sphere with the same circumference as the rough grain, calculated using the circumference c_g of the rough grain: $L = c_g/2\pi$. Thus, we obtain an equivalent radius L, which we substitute into Equation 34.

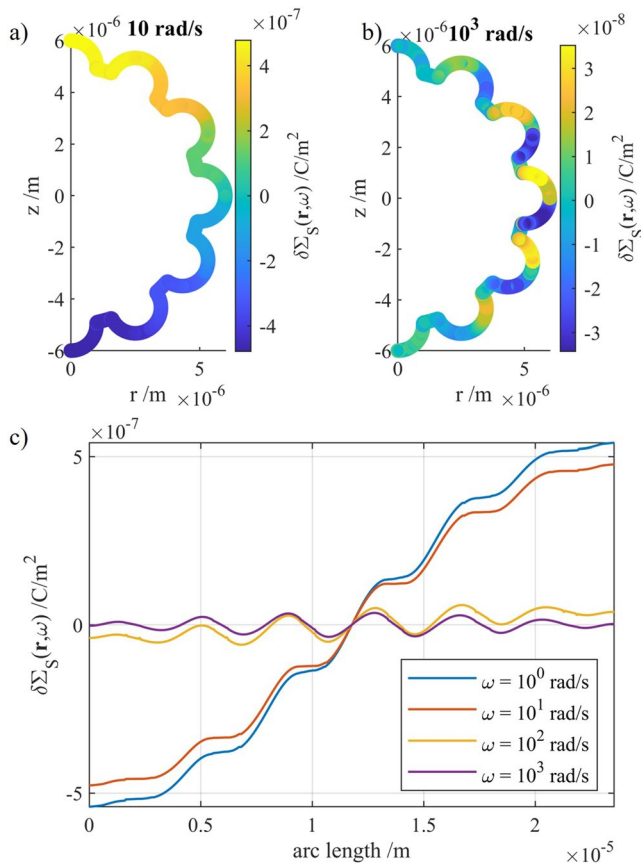$$\tau = \left(\frac{c_g}{2\pi}\right)^2 / 2D_S M \tag{36}$$

Figure 9. Stern layer charge perturbation at (a) 10 rad/s and (b) 1,000 rad/s of a fractal grain model. The applied electric field is pointing upward, that is, it is parallel to the vertical axis. (c) Stern layer charge perturbation as a function of arc length along the surface displayed in (a and b).

With this, our rough models perfectly match the trend predicted by Equation 36 confirming the dependence of the primary relaxation time of rough grains on polarization length (Figures 8c and 8d).

In addition to shifting the primary polarization peak, surface roughness leads to additional polarizations at higher frequencies (Figure 5 through 7). We associate these additional polarizations with the tiny structures, that is, short relaxation lengths (and thus times), on the rough surfaces. This is best seen for fractal grains, where one and two daughter generations give rise to one and two polarization peaks, respectively (Figure 5). To confirm or reject this interpretation, we look at the perturbation of the Stern layer charge density.

Figure 9 shows the Stern layer surface charge perturbation at four different frequencies. Figures 9a and 9b show it along the model surface for $\omega = 10$ rad/s and $\omega = 10^3$ rad/s, respectively, with the electric field parallel to the vertical axis. The Stern layer charge perturbation shows surpluses (yellow) and deficits (blue). The magnitude of the perturbation decreases with increasing frequency from about 5×10^{-7} C/m^2 (Figures 9a) to 3.5×10^{-8} C/m^2 (Figure 9b). At $\omega = 10$ rad/s, the surface charge perturbation shows a gradient across the grain surface (Figure 9a), that is, the entire grain is polarized. At 10^3 rad/s, the large-scale gradient disappears and gradients at each small daughter structure dominate. This is reflected in the imaginary conductivity spectrum of this model (Figure 5a): the primary peak corresponds to the large-scale polarization of the whole grain around 1 rad/s, and the secondary peak represents the small-scale polarizations of the daughter structures between 10^2 and 10^4 rad/s. Figure 9c shows the Stern layer charge perturbation as a function of arc length for four different frequencies, including those shown in Figures 8a and 8b. The red line ($\omega = 10$ rad/s) corresponds to the primary peak frequency. The surface charge perturbation takes negative values at the beginning (bottom side of the grain) and increases steadily with distance until it reaches the end (top side of the grain). Halfway through (right side of the grain) we see a change in polarity, where all the lines overlap. Blue ($\omega = 1$ rad/s) and red ($\omega = 10$ rad/s) lines show the surface charge perturbation just before and at the polarization peak of the primary (large-scale) polarization. Although the effects of the smaller structures are visible in the plot (oscillations), they play a minor role compared to the effects over the entire arc length. This changes drastically when we reach the onset of the secondary polarization ($\omega = 100$ rad/s, yellow line). The large-scale gradient almost disappears and the small-scale perturbations start to dominate. At the peak frequency of the secondary polarization ($\omega = 1,000$ rad/s, purple line), the large-scale perturbation becomes negligible, and the line oscillates around $\delta\Sigma_S = 0$ C/m^2. For both high frequencies (10^2 and 10^3 rad/s) we can see an increase of the small-scale perturbations from the edges to the center.

5.2. Influence of Surface Roughness on Polarization Magnitude

In Figure 10a, we compare the normalized chargeability obtained for our models, plotted against S_{por}, with the results of an empirical study on natural sandstone samples (solid line) and unconsolidated sand-clay mixtures (dashed line) by Weller et al. (2010). Our results follow the empirical trends, that is, have the same slope as the laboratory data, but have slightly lower chargeabilities.

Figure 10b shows the imaginary conductivity σ'' at 1 Hz versus S_{por}. Again, we compare our simulation results with measurements on sandstone samples and unconsolidated sand-clay mixtures (Weller et al., 2010). Since we are considering the polarization at 1 Hz, we are interested in the grain size that has its relaxation frequency at 1 Hz. The relaxation time τ and the angular frequency ω are related by $\tau = 1/\omega$. Together with Equation 31, we obtain the relationship between polarization frequency and grain radius:

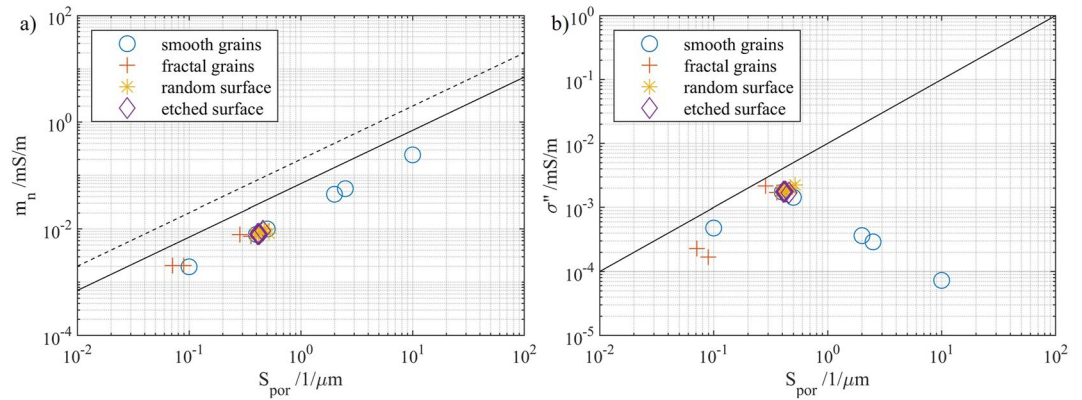$$\omega = \frac{2 D_S M}{r^2} \tag{37}$$

Figure 10. Comparison of simulation results (symbols) to the empirical behavior of sandstones (solid line) and unconsolidated sand-clay mixtures (dashed line) from Weller et al. (2010) for (a) normalized chargeability m_n versus inner surface area relative to pore volume S_{por}, and (b) σ'' at 1 Hz versus S_{por}.

Given $\omega = 2\pi f$, grains with radii of 2–20 μm will have a polarization frequency around frequencies of $f = 0.1-10$ Hz. Smaller and larger grains would polarize at higher and lower frequencies, respectively. Consequently, only the models with grain radii in this range, that is, the 20 and 5 μm models produce signals in the relevant frequency range. Our smaller models polarize at much higher frequencies and, therefore, have a low σ'' around 1 Hz.

5.3. Effect of Model Symmetry

The results presented show the influence of surface roughness on the SIP response of grain models. However, even our models with random surface roughness are unnatural due to their axis symmetry (Figures 3 and 4). Since the symmetry axis is parallel to the applied electric field, all ions moving along the particle surface traverse the same topographic profile, that is, each polarization caused by a particular structural feature is emphasized. Consequently, the fractal models with one or two daughter generations, that is, with surface structures of one or two length scales, show one or two distinct peaks above the primary peak frequency, respectively. For non-axisymmetric fractal grains, the ions moving along the surface would traverse different topographic profiles. Thus, we expect a broadening of the secondary peaks for non-symmetric rough surfaces.

5.4. Comparison With Experimental Data

Leroy et al. (2008) observed similar behavior in their experiments on packs of smooth and rough glass beads packs. Their figure 14 shows the phase spectra of a smooth bead pack and a rough bead pack, as well as images of the bead surface. The smooth bead packs appear to have some minor surface roughness (dark spots in the image) which produces a secondary polarization between $10-10^3$ Hz (Leroy et al., 2008). After acid treatment, the bead surface becomes noticeably rougher, existing cavities are further eroded, and numerous new cavities appear in the rough bead image (see their Figure 14). The phase spectrum shows the expected behavior, with the polarization flattening and extending over a wider frequency range. Contrary to our models, the primary polarization of the rough bead pack increases in magnitude.

Consequently, even though axis symmetry introduces a flaw to our models, our results enable us to qualitatively predict the effects of surface roughness on the SIP response. A non-axisymmetric model domain would allow the creation of surfaces with variations in two dimensions. However, such a true 3D model requires a very large computational grid and exceeds the computing power of the computers used. Even on a cluster, parameter studies would not be possible due to the high number of grid elements.

5.5. Effect of Increased Surface Roughness on S_{por}

The particle volume determines the bulk volume of the model domain because we keep the volumetric content of the solid fraction constant for all models. Eventually, the S_{por} of all our models is mainly controlled by the ratio

of the surface area to the bulk volume of the model (Equations 29 and 30)). We have presented two approaches to generate surface roughness. For the fractal models, we add material to the existing smooth surface. With the random models, the amplitude associated with a normal distribution function that produces values around a zero mean (3.1.2) determines whether material is added to or subtracted from the smooth surface. By modifying the mathematical parameterization, we can take control over the preferred direction of oscillation and choose whether material is added or removed.

Consequently, with the fractal approach, we continue to increase the particle volume with each addition of smaller particles. The fractal model with one daughter generation grows in volume by 41%, while two daughter generations increase the particle volume by 52%. The random models don't change as much, growing in volume by up to 8%, and the preferred direction models gain or lose up to 4% compared to the volume of the smooth particle. The surface area increases by 66% and 127% for the two fractal models and by up to 40% for the random models. However, the fractal models all have lower S_{por} than the random models because they gain more volume per increase in surface area.

5.6. Ambiguity of IP Spectra

Despite the shortcomings of our models, we assume that our results regarding the influence of surface roughness on the SIP response are still applicable to rocks. In this sense, we see an ambiguity in the interpretation of IP spectra. Mechanistic grain polarization models have been and are being used to derive grain size distributions from SIP measurements (e.g., Revil & Florsch, 2010). These approaches assume that the distribution of relaxation time is transferable to a grain size distribution. However, as Leroy et al. (2008) already have shown in laboratory experiments and supported by our simulation results, this assumption is not universal. Surface roughness causes additional polarization in the frequency range above the primary polarization. Consequently, the interpretation of a SIP response with a broad secondary peak is ambiguous, since a set of equally sized, rough grains and sets of differently sized grains can produce a similar SIP response.

6. Summary and Conclusion

Previous publications indicate that S_{por} plays an important role in the SIP response of rocks (Weller et al., 2010). In order to better understand the SIP signals measured on rocks, we have numerically investigated the influence of surface roughness on the SIP response of grain models. Since the introduction of surface roughness has a direct effect on S_{por}. To increase the surface roughness, we chose two different approaches: (a) we assembled fractal grains from self-similar geometries, and (b) we used harmonic functions in conjunction with random number generators for more natural looking surfaces. We numerically solved the NPP equations, which we used to describe the polarization of the EDL at the solid-electrolyte-interface, to simulate the SIP response. Finally, we compared the SIP parameter of the simulation results with those of empirical and mechanistic models.

We find that, with few exceptions, the behavior of our models is in good agreement with observations from laboratory measurements (Andreas Weller et al., 2010; Leroy et al., 2008). Our simulations of smooth and rough grains follow the trend of the $S_{por}-m_n$ relationship. However, models of smaller particles with $r_p < 5$ μm do not reproduce the empirically found $S_{por} - \sigma''_{1\,Hz}$ relationship. This is mainly due to the nature of our simulation, which only considers the polarization of the EDL around single grains, which polarize for these small grains at frequencies significantly above 1 Hz. Moreover, our simulations neglect mechanisms such as grain-grain interactions, membrane polarization at pore constrictions, or overlapping EDLs, all of which may contribute to the polarization around 1 Hz. The tiny structures on rough surfaces as well as most of our grains have smaller polarization lengths and thus higher polarization frequencies. Therefore, without interaction with adjacent charged surfaces they contribute little or nothing to the polarization at 1 Hz. Volkmann and Klitzsch (2016) observed a similar behavior in SIP measurements on sintered glass samples consisting only of certain grain sizes. They found a strong frequency dependence of the correlation between imaginary conductivity and inner surface area for these samples.

We identified the following effects of surface roughness on the SIP response. First, we observed a shift of the primary polarization frequency to lower frequencies and lower magnitudes. The primary peak frequency is mainly controlled by the relaxation path length along the particle surface. This path length increases as the intensity of the surface roughness increases. Second, we observed an increase of σ'' behind the primary peak up to the

formation of secondary polarization peaks (fractal models). These secondary polarizations occur at the smaller surface structures (Figure 9).

The SIP method is sensitive to inner surface roughness with characteristic surface structure lengths down to a few hundred nanometers. Thus, SIP has the potential to measure the inner surface roughness by interpreting the secondary polarizations caused by the rough inner surface. However, such an interpretation would be ambiguous because, for example, the SIP response of a suspension of similarly sized, rough particles cannot be distinguished from a suspension of particles following a particular particle size distribution.

Data Availability Statement

Scripts, numerical models, and data used for this manuscript are available at Zenodo (Zibulski & Klitzsch, 2022).

References

Archie, G. E. (1942). The electrical resistivity log as an aid in determining some reservoir characteristics. *Transactions of the AIME*, *146*(01), 54–62. https://doi.org/10.2118/942054-G

Atekwana, E. A., & Slater, L. D. (2009). Biogeophysics: A new Frontier in Earth science research. *Reviews of Geophysics*, *47*(4). https://doi.org/10.1029/2009RG000285

Blaschek, R., & Hördt, A. (2009). Numerical modelling of the IP effect at the pore scale. *Near Surface Geophysics*, *7*(5–6), 579–588. https://doi.org/10.3997/1873-0604.2009030

Bücker, M., Flores Orozco, A., Undorf, S., & Kemna, A. (2019). On the role of Stern- and diffuse-layer polarization mechanisms in porous media. *Journal of Geophysical Research: Solid Earth*, *124*(6), 5656–5677. https://doi.org/10.1029/2019JB017679

Bücker, M., & Hördt, A. (2013a). Analytical modelling of membrane polarization with explicit parametrization of pore radii and the electrical double layer. *Geophysical Journal International*, *194*(2), 804–813. https://doi.org/10.1093/gji/ggt136

Bücker, M., & Hördt, A. (2013b). Long and short narrow pore models for membrane polarization. *Geophysics*, *78*(6), E299–E314. https://doi.org/10.1190/geo2012-0548.1

Chapman, D. L. (1913). LI. A contribution to the theory of electrocapillarity. *The London, Edinburgh and Dublin Philosophical Magazine and Journal of Science*, *25*(148), 475–481. https://doi.org/10.1080/14786440408634187

Chen, Y., & Or, D. (2006). Effects of Maxwell-Wagner polarization on soil complex dielectric permittivity under variable temperature and electrical conductivity. *Water Resources Research*, *42*(6). https://doi.org/10.1029/2005WR004590

Chew, W. C., & Sen, P. N. (1982a). Dielectric enhancement due to electrochemical double layer: Thin double layer approximation. *The Journal of Chemical Physics*, *77*(9), 4683–4693. https://doi.org/10.1063/1.444369

Chew, W. C., & Sen, P. N. (1982b). Potential of a sphere in an ionic solution in thin double layer approximations. *The Journal of Chemical Physics*, *77*(4), 2042–2044. https://doi.org/10.1063/1.444060

Cole, K. S., & Cole, R. H. (1941). Dispersion and absorption in dielectrics I. Alternating current characteristics. *The Journal of Chemical Physics*, *9*(4), 341–351. https://doi.org/10.1063/1.1750906

Dukhin, S. S., Shilov, V. N., & Bikerman, J. J. (1974). Dielectric phenomena and double layer in disperse systems and polyelectrolytes. *Journal of the Electrochemical Society*, *121*(4), 154C. https://doi.org/10.1149/1.2402374

Flores Orozco, A., Williams, K. H., Long, P. E., Hubbard, S. S., & Kemna, A. (2011). Using complex resistivity imaging to infer biogeochemical processes associated with bioremediation of an uranium-contaminated aquifer. *Journal of Geophysical Research*, *116*(G3), G03001. https://doi.org/10.1029/2010JG001591

Gouy, M. (1910). Sur la constitution de la charge électrique à la surface d'un électrolyte. *Journal De Physique Théorique Et Appliquée*, *9*(1), 457–468. https://doi.org/10.1051/jphystap:019100090045700

Grahame, D. C. (1947). The electrical double layer and the theory of electrocapillarity. *Chemical Reviews*, *41*(3), 441–501. https://doi.org/10.1021/cr60130a002

Helmholtz, H. (1853). Ueber einige Gesetze der Vertheilung elektrischer Ströme in körperlichen Leitern, mit Anwendung auf die thierisch-elektrischen Versuche (Schluss.). *Annalen Der Physik Und Chemie*, *165*(7), 353–377. https://doi.org/10.1002/andp.18531650702

Hördt, A., Druiventak, A., Blaschek, R., Binot, F., Kemna, A., Kreye, P., & Zisser, N. (2009). Case histories of hydraulic conductivity estimation with induced polarization at the field scale. *Near Surface Geophysics*, *7*(5–6), 529–545. https://doi.org/10.3997/1873-0604.2009035

Kremer, F. & Schönhals, A. (Eds.) (2003). *Springer eBook collection. Broadband dielectric spectroscopy*. Springer Berlin Heidelberg. https://doi.org/10.1007/978-3-642-56120-7

Leroy, P., & Revil, A. (2009). A mechanistic model for the spectral induced polarization of clay materials. *Journal of Geophysical Research*, *114*(B10), B10202. https://doi.org/10.1029/2008JB006114

Leroy, P., Revil, A., Kemna, A., Cosenza, P., & Ghorbani, A. (2008). Complex conductivity of water-saturated packs of glass beads. *Journal of Colloid and Interface Science*, *321*(1), 103–117. https://doi.org/10.1016/j.jcis.2007.12.031

Lesmes, D. P., & Morgan, F. D. (2001). Dielectric spectroscopy of sedimentary rocks. *Journal of Geophysical Research*, *106*(B7), 13329–13346. https://doi.org/10.1029/2000JB900402

Lyklema, J., Dukhin, S. S., & Shilov, V. N. (1983). The relaxation of the double layer around colloidal particles and the low-frequency dielectric dispersion. *Journal of Electroanalytical Chemistry and Interfacial Electrochemistry*, *143*(1–2), 1–21. https://doi.org/10.1016/S0022-0728(83)80251-4

Marshall, D. J., & Madden, T. R. (1959). Induced polarization, a study of its causes. *Geophysics*, *24*(4), 790–816. https://doi.org/10.1190/1.1438659

Mellage, A., Smeaton, C. M., Furman, A., Atekwana, E. A., Rezanezhad, F., & van Cappellen, P. (2018). Linking spectral induced polarization (SIP) and subsurface microbial processes: Results from sand column incubation experiments. *Environmental Science and Technology*, *52*(4), 2081–2090. https://doi.org/10.1021/acs.est.7b04420

Nordsiek, S., & Weller, A. (2008). A new approach to fitting induced-polarization spectra. *Geophysics*, *73*(6), F235–F245. https://doi.org/10.1190/1.2987412

O'Konski, C. T. (1960). Electric properties of macromolecules. V. theory of ionic polarization in polyelectrolytes. *Journal of Physical Chemistry*, *64*(5), 605–619. https://doi.org/10.1021/j100834a023

Pelton, W. H., Ward, S. H., Hallof, P. G., Sill, W. R., & Nelson, P. H. (1978). Mineral discrimination and removal of inductive coupling with multifrequency IP. *Geophysics*, *43*(3), 588–609. https://doi.org/10.1190/1.1440839

Revil, A. (2013). Effective conductivity and permittivity of unsaturated porous materials in the frequency range 1 mHz-1GHz. *Water Resources Research*, *49*(1), 306–327. https://doi.org/10.1029/2012WR012700

Revil, A., & Florsch, N. (2010). Determination of permeability from spectral induced polarization in granular media. *Geophysical Journal International*. Advance online publication. https://doi.org/10.1111/j.1365-246X.2010.04573.x

Revil, A., & Glover, P. W. J. (1998). Nature of surface electrical conductivity in natural sands, sandstones, and clays. *Geophysical Research Letters*, *25*(5), 691–694. https://doi.org/10.1029/98GL00296

Revil, A., Koch, K., & Holliger, K. (2012). Is it the grain size or the characteristic pore size that controls the induced polarization relaxation time of clean sands and sandstones? *Water Resources Research*, *48*(5). https://doi.org/10.1029/2011WR011561

Revil, A., & Skold, M. (2011). Salinity dependence of spectral induced polarization in sands and sandstones. *Geophysical Journal International*, *187*(2), 813–824. https://doi.org/10.1111/j.1365-246X.2011.05181.x

Schlumberger, C. (1920). *Étude sur la prospection électrique du sous-sol*. Gauthier-Villars.

Schurr, J. M. (1964). On the theory of the dielectric dispersion of spherical colloidal particles in electrolyte solution 1. *Journal of Physical Chemistry*, *68*(9), 2407–2413. https://doi.org/10.1021/j100791a004

Schwarz, G. (1962). A theory of the low-frequency dielectric dispersion of colloidal particles in electrolyte solution 1,2. *Journal of Physical Chemistry*, *66*(12), 2636–2642. https://doi.org/10.1021/j100818a067

Sen, P. N., Scala, C., & Cohen, M. H. (1981). A self-similar model for sedimentary rocks with application to the dielectric constant of fused glass beads. *Geophysics*, *46*(5), 781–795. https://doi.org/10.1190/1.1441215

Sjodin, B. (2017). *How to generate random surfaces in COMSOL Multiphysics®*. COMSOL. Retrieved from https://www.comsol.com/blogs/how-to-generate-random-surfaces-in-comsol-multiphysics/

Stern, O. (1924). Zur Theorie der Elektrolytischen Doppelschicht. *Zeitschrift Für Elektrochemie*, *30*(21–22), 508–516.

Strobel, C., Abramov, S., Huisman, J. A., Cirpka, O. A., & Mellage, A. (2023). Spectral induced polarization (SIP) of denitrification-driven microbial activity in column experiments packed with calcareous aquifer sediments. *Journal of Geophysical Research: Biogeosciences*, *128*(1). https://doi.org/10.1029/2022JG007190

Telford, W. M., Geldart, L. P., & Sheriff, R. E. (1990). *Applied geophysics* (2nd). Cambridge University Press.

Titov, K., Komarov, V., Tarasov, V., & Levitski, A. (2002). Theoretical and experimental study of time domain-induced polarization in water-saturated sands. *Journal of Applied Geophysics*, *50*(4), 417–433. https://doi.org/10.1016/S0926-9851(02)00168-4

Volkmann, J., & Klitzsch, N. (2010). Frequency-dependent electric properties of microscale rock models for frequencies from one millihertz to ten kilohertz. *Vadose Zone Journal*, *9*(4), 858–870. https://doi.org/10.2136/vzj2009.0162

Volkmann, J., & Klitzsch, N. (2016). Evaluation of low frequency polarization models using well characterized sintered porous glass samples. *Journal of Applied Geophysics*, *124*, 39–53. https://doi.org/10.1016/j.jappgeo.2015.11.011

Weller, A., & Börner, F. D. (1996). Measurements of spectral induced polarization for environmental purposes. *Environmental Geology*, *27*(4), 329–334. https://doi.org/10.1007/BF00766702

Weller, A., & Breede, K. (2006). Multi-salinity measurements of spectral induced polarisation on sandstones. In *Near surface 2006 - 12th EAGE European Meeting of Environmental and Engineering Geophysics*. European Association of Geoscientists and Engineers. https://doi.org/10.3997/2214-4609.201402696

Weller, A., Slater, L., Nordsiek, S., & Ntarlagiannis, D. (2010). On the estimation of specific surface per unit pore volume from induced polarization: A robust empirical relation fits multiple data sets. *Geophysics*, *75*(4), WA105–WA112. https://doi.org/10.1190/1.3471577

Wong, J. (1979). An electrochemical model of the induced-polarization phenomenon in disseminated sulfide ores. *Geophysics*, *44*(7), 1245–1265. https://doi.org/10.1190/1.1441005

Zibulski, E., & Klitzsch, N. (2022). Influence of inner surface roughness on the SIP response - a numerical study. https://doi.org/10.5281/ZENODO.7049722